2011

An Integrated Thermal and Mechanical Investigation of Molten-Salt Thermocline Energy Storage

S. Flueckiger
Purdue University - Main Campus

Z. Yang
Purdue University - Main Campus

S V. Garimella
Purdue University, sureshg@purdue.edu

Flueckiger, S.; Yang, Z.; and Garimella, S V., "An Integrated Thermal and Mechanical Investigation of Molten-Salt Thermocline Energy Storage" (2011). *CTRC Research Publications*. Paper 150.
http://dx.doi.org/10.1016/j.apenergy.2010.12.031

An Integrated Thermal and Mechanical Investigation of Molten-Salt Thermocline Energy Storage*

Scott Flueckiger[1], Zhen Yang[2], and Suresh V. Garimella[1]**

[1]School of Mechanical Engineering

Cooling Technologies Research Center, an NSF IUCRC

585 Purdue Mall, Purdue University

West Lafayette, IN 47907-2088 USA

[2] Key Laboratory for Thermal Science and Power Engineering of Ministry of Education

Department of Thermal Engineering

Tsinghua University

Beijing 100084 China

* Submitted for publication in *Applied Energy*, July 2010, and in revised form, September 2010
** Author to whom correspondence should be addressed: (765) 494-5621, sureshg@purdue.edu

Abstract

Thermal ratcheting is a critical phenomenon associated with the cyclic operation of dual-medium thermocline tanks in solar energy applications. Although thermal ratcheting poses a serious impediment to thermocline operation, this failure mode in dual-medium thermocline tanks is not yet well understood. To study the potential for the occurrence of ratcheting, a comprehensive model of a thermocline tank that includes both the heterogeneous filler region as well as the composite tank wall is formulated. The filler region consists of a rock bed with interstitial molten salt, while the tank wall is composed of a steel shell with two layers of insulation (firebrick and ceramic). The model accounts separately for the rock and molten salt regions in view of their different thermal properties. Various heat loss conditions are applied at the external tank surface to evaluate the effect of energy losses to the surroundings. Hoop stresses, which are governed by the magnitude of temperature fluctuations, are determined through both a detailed finite element analysis and simple strain relations. The two methods are found to yield almost identical results. Temperature fluctuations are damped by heat losses to the surroundings, leading to a reduction in hoop stresses with increased heat losses. Failure is prevented when the peak hoop stress is less than the material yield strength of the steel shell. To avoid ratcheting without incurring excessive energy loss, insulation between the steel shell and the filler region should be maximized.

Keywords: Solar thermal energy, thermal energy storage, molten-salt thermocline, thermal ratcheting

1. Introduction

Concentrated Solar Thermal (CST) power plants [1-6] have been identified as a promising renewable option for the economical generation of electricity at a large scale. The use of a molten-salt thermocline for thermal energy storage (TES) in a CST power plant is believed to lead to a potential reduction in capital cost of 35% relative to a two-tank counterpart [7,8]. In a molten-salt thermocline, a molten salt (e.g., HITEC or HITEC XL [9]) is used as the heat transfer fluid (HTF) that transports thermal energy between the storage unit and the other sections of the power system such as the collector field and the steam generator. Separation between the hot and cold zones of the molten salt is maintained by a thin slice of the tank which experiences a large temperature gradient, known as the thermocline or heat exchange region. This region is naturally enabled by buoyancy forces and preserves stable thermal stratification of the fluid in the tank. To reduce the inventory of relatively expensive molten salt in the storage system, a low-cost filler material compatible with molten salts, such as quartzite rock [10], is used to fill much of the volume in the thermocline tank and acts as the primary thermal storage material. Thermoclines of this type are termed dual-media or multi-media storage systems. A detailed experimental demonstration of a dual-media thermocline on a pilot scale (2.3 MWh) was reported in [11].

Despite its advantage in terms of cost, stability of the filler material in the hot molten-salt environment as well as thermomechanically induced ratcheting are important concerns that need attention in the design and operation of dual-media thermoclines. The first of these concerns is addressed by appropriate choice of compatible filler material such as quartzite rock and silica sand for nitrate salts (HITEC and HITEC XL). The thermal ratcheting problem, on the other hand, requires a comprehensive understanding of the combined thermal and mechanical characteristics of the tank and is the focus of the present work.

Thermal ratcheting is an important design issue in multiple applications [12,13], but has not been extensively studied for dual-media thermoclines, in which thermal ratcheting can occur when the system undergoes successive charge and discharge cycles. As the tank heats up during the charge cycle, its internal volume increases and the filler particles settle lower to fill the additional volume created by the thermal expansion; as the tank cools down during the discharge cycle, however, the filler particles cannot be displaced upward due to gravity, inter-particle friction and resistance from particle packing. This prevents the tank wall from shrinking to its original dimensions, resulting in a build-up of mechanical stress in the tank shell through repeated operational cycles. If the stress in the tank shell reaches the yield point, plastic deformation occurs. Further cycling can then lead to structural failure of the tank.

The largest thermocline facility to be constructed to date was the 10 MWe tank integrated into the Solar One pilot plant [14]. A central receiver plant with direct steam generation, the Solar One thermocline was an indirect storage system with synthetic oil (Caloria HT-43) used as the HTF. Due to insufficient heliostats for excess solar harvesting, use of the storage subsystem was sporadic and primarily provided auxiliary steam generation. Under these conditions of use, thermal ratcheting was determined not to be a potential failure mode as the thermal expansion of the filler material exceeded that of the carbon steel wall. Stresses in the tank wall were monitored with strain gages to verify this assessment, but did suffer from large uncertainty in the strain measurements.

It should be noted that the potential for thermal ratcheting is intimately related to the heat transfer, tank structure, and materials used in thermocline systems, and depends on the design and operational characteristics. It is important that both thermal and mechanical considerations be investigated to ensure the absence of a potential for ratcheting.

An integrated analysis of the thermal and mechanical behavior of thermocline tanks of different wall structures under different heat transfer boundaries is conducted in the present study. The molten-salt flow and heat transfer in the tank are simulated by a two-temperature model to account for the different thermal properties of the filler material and the salt; heat transfer in the tank shell is included and is coupled with the molten-salt flow in the tank. The resulting thermomechanical stress used for the prediction of thermal ratcheting is analyzed using both finite element analysis and simple analytical strain relations. With this modeling approach, the potential for thermal ratcheting of a thermocline tank is investigated for various composite tank wall thicknesses and surface boundary conditions.

2. Numerical Modeling

2.1 Problem Description

A schematic representation of a TES thermocline tank is provided in Fig. 1. The tank of inner diameter *d* is filled with a porous bed of quartzite rock to a height *h*. A molten salt (HITEC [15]) serves as the heat transfer fluid (HTF) and flows through the filler bed to exchange heat with the quartzite filler. The density, viscosity, and thermal conductivity of the HITEC fluid are defined by the following temperature-dependent functions [16] derived from experimental data [15]:

$$\rho_l(T) = 1938 - 0.732\left(T_l - 200\right) \tag{1}$$

$$\mu(T) = \exp\left[-4.343 - 2.0143\left(\ln(T_l) - 5.011\right)\right] \tag{2}$$

$$k_l(T) = -0.000653\left(T_l - 260\right) + 0.421 \tag{3}$$

The specific heat of HITEC is 1561.7 J/kg-K, while the density and specific heat of quartzite rock are 2201 kg/m^3 and 964 J/kg-K, respectively. The effective thermal conductivity of the

dual-media mixture is computed using the correlation proposed by Gonzo [17]. The porosity of the filler region is assumed to be 0.22 with an average filler particle size of 0.05 m.

In this work, the tank dimensions d and h are set to be equal although there are many other options for tall ($d < h$) and flat ($d > h$) thermocline systems. Above and below the porous filler bed are distributors of height h' ($h' = 0.05h$), which are free of quartzite rock. These distributor regions serve to maintain a uniform flow condition at both ends of the filler bed in order to achieve good thermal stratification. The distributors are connected to the rest of the system with tubes of diameter d' ($d' = 0.05d$) at the top and bottom ports.

During the charge cycle, a hot molten-salt flow at a high temperature level T_h from the collector field is pumped through the top port into the tank, heating up and thus storing solar heat in the filler particles; during the discharge cycle, a cold molten-salt flow at a lower temperature level T_c is pumped through the bottom port into the tank, heated by the hot filler particles and exhausted from the top port. As the discharge period commences, molten-salt outflow through the top port is maintained at the desired high temperature level, and is delivered for generating superheated steam for electricity production. As the discharge process continues, the outflow decreases in temperature, eventually falling to a value that is no longer suitable for generating steam. As a result, only a portion of the initially stored thermal energy can be retrieved as useful heat.

The tank considered here has a complex wall consisting of multiple layers [18,19]: an inner firebrick layer for thermal isolation, a steel shell layer for mechanical support and an outer layer of ceramic fiber for corrosion protection and thermal insulation. To inhibit leakage of the molten salt through the internal insulation, a thin liner material is installed between the rock and insulation. The liner is corrugated to accommodate thermal expansion and contraction

associated with the operation of the thermocline. The length scale of these corrugations is assumed to be smaller than the size of the granular filler, inhibiting full contact with the rock and preventing crushing of the liner. Due to the small relative thickness of the corrugated liner, its thermal effects are neglected.

Relevant thermal transport properties for the two insulation materials and structural shell are listed in Table 1. The tank is built on a concrete foundation which is cooled by embedded water tubes; its side and top walls are exposed to atmosphere. Therefore, the thermal boundary conditions on the external wall of the tank are set to a mixed convection and radiation heat transfer condition on the exposed walls, and a constant temperature condition on the bottom wall.

2.2 Governing Equations

(a) Molten-salt flow and heat transfer inside thermocline tank

Mass and momentum transport of the molten salt in the fillerbed are governed by [16]:

$$\frac{\partial(\varepsilon\rho_l)}{\partial t} + \nabla\cdot\left(\rho_l \vec{u}\right) = 0 \tag{4}$$

$$\frac{\partial(\varepsilon\rho_l)}{\partial t} + \nabla\cdot\left(\rho_l \frac{\vec{u}\vec{u}}{\varepsilon}\right) = -\varepsilon\nabla\cdot p + \nabla\cdot\vec{\vec{\tau}} + \varepsilon\rho_l\vec{g} - \varepsilon\left(\frac{\mu}{K}\vec{u} + \frac{F}{\sqrt{K}}\rho_l|\vec{u}|\vec{u}\right) \tag{5}$$

The stress tensor is defined as $\vec{\vec{\tau}} = 2\mu\vec{\vec{S}} - \frac{2}{3}\mu S_{kk}\vec{\vec{I}}$, where $\vec{\vec{S}} = \frac{1}{2}\left(\nabla\vec{u} + (\nabla\vec{u})^T\right)$. The spatial gradient for polar coordinates is $\nabla = \vec{e}_r\frac{\partial}{\partial r} + \vec{e}_\theta\frac{1}{r}\frac{\partial}{\partial\theta} + \vec{e}_x\frac{\partial}{\partial x}$, although the axisymmetric assumption for the thermocline operation in this work eliminates any dependency in the circumferential direction (θ). In contrast to the fillerbed, molten-salt flow in the tank distributors is turbulent. To account for this local turbulence, the standard k-ε model is enforced in the distributor regions [20].

For the two-temperature model with co-located data storage, the energy transport equations for the molten salt (subscripted *l*) and the solid filler (subscripted *s*) provided below are coupled by the interstitial heat transfer. The interstitial heat transfer coefficient, h_i, is computed from the Nusselt number (*Nu*) associated with this inter-phase exchange which is obtained from the correlation of Wakao and Kaguei for forced convection inside a packed bed [21].

$$\frac{\partial\left[\varepsilon\rho_l C_{P,l}\left(T_l - T_c\right)\right]}{\partial t} + \nabla\cdot\left[\rho_l \vec{u} C_{P,l}\left(T_l - T_c\right)\right] = \nabla\cdot\left(k_e \nabla T_l\right) + p\nabla\cdot\vec{u} + tr\left[\nabla\left(\frac{\vec{u}}{\varepsilon}\right)\cdot\bar{\bar{\tau}}\right] + \frac{\vec{u}\cdot\vec{u}}{2\varepsilon}\times\frac{\partial\rho_l}{\partial t} + h_i\left(T_s - T_l\right) \tag{6}$$

$$\frac{\partial}{\partial t}\left[(1-\varepsilon)\rho_s C_{P,s}\left(T_s - T_c\right)\right] = -h_i\left(T_s - T_l\right) \tag{7}$$

Each of the governing transport equations can be readily non-dimensionalized, as presented in the literature [16,22].

(b) Boundary conditions

During discharge of the thermocline tank, molten salt enters the bottom distributor at a fixed velocity and temperature:

$$\vec{u} = \left(\frac{d}{d'}\right)^2 u_m \vec{e}_x,\ T = T_c \tag{8}$$

At the outflow from the upper thermocline distributor:

$$\frac{\partial \vec{u}}{\partial x} = 0,\ \frac{\partial T}{\partial x} = 0 \tag{9}$$

Due to the elevated temperatures of the molten salt, the ceramic exterior of the thermocline tank experiences heat exchange with the surroundings by both convection and radiation:

$$\left.\frac{\partial T_3}{\partial r}\right|_w = -\frac{h_w}{k_3}\left(T_w - T_\infty\right) - \frac{\varepsilon_w \sigma_r}{k_3}\left(T_w{}^4 - T_\infty{}^4\right) \tag{10}$$

(c) Heat conduction in composite wall

While convection and radiation occur at the tank surface, heat is transported by conduction in each layer of the composite wall according to the heat diffusion equation with properties inserted appropriately for each layer:

$$\rho C_P \frac{\partial T}{\partial t} = -k\nabla \cdot T \tag{11}$$

To account for heat transfer at the two solid interfaces (firebrick and steel, steel and ceramic), the following heat balance is applied:

$$\left.\frac{\partial T_1}{\partial r}\right|_{12} = \frac{k_2}{k_1}\left.\frac{\partial T_2}{\partial r}\right|_{12}, \quad \left.\frac{\partial T_2}{\partial r}\right|_{23} = \frac{k_3}{k_2}\left.\frac{\partial T_3}{\partial r}\right|_{23} \tag{12}$$

(d) Mechanical stress

All solid materials experience some finite change in volume when exposed to an increase in temperature. The steel tank shell can expand or contract freely in the height direction as no structural restrictions are applied in this direction; *in the circumferential direction, however, deformation is determined by the maximum temperature experienced at each axial location and then holds constant (as explained below) provided the yield stress of the material has not been exceeded.* The possibility of thermal ratcheting (which occurs upon plastic deformation of the shell) must thus be investigated only in the circumferential direction, henceforth referred to as the principal direction. In the principal direction, the amount of change or strain is composed of two parts: thermal strain ε_T and mechanical strain ε_M, represented as:

$$\varepsilon_L(x,r) = \varepsilon_T + \varepsilon_M \tag{13}$$

The thermal strain is dependent on the coefficient of thermal expansion (α_L) for the given material:

$$\varepsilon_T(x,r) = \alpha_L \left[T_2(x,r) - T_{ref} \right] \tag{14}$$

The mechanical strain is related to the modulus of elasticity (E) of the steel and the principal stress (σ):

$$\varepsilon_M(x,r) = \frac{\sigma}{E} \tag{15}$$

The weight of the filler bed and molten salt in the tank exerts pressure on the tank wall, inducing a certain amount of mechanical stress in the steel tank shell. However this stress (~10^5 Pa) is negligible compared to that caused by tank contraction (~10^7-10^8 Pa).

When the steel tank wall is heated to its maximum temperature in a charge cycle, the thermal strain also reaches its maximum. Since the filler region does not prevent expansion and the tank wall can expand freely, the mechanical strain ε_M remains at zero, resulting in the total strain of the tank being solely that due to thermal strain, as shown in Eq. (13). Strain interaction with the firebrick and ceramic sections is neglected as these layers are composed of loosely connected blocks, and are therefore unable to provide structural support to the filler region. In any case, if the filler imposes an unacceptable level of stress on the firebrick, an alternative insulation material may be substituted with similar thermal properties, such as thermal wool. The term “firebrick” is used here in a generic sense, and does not refer to a specific material.

While the filler medium settles into the expanded volume, it cannot be dislodged upward to allow contraction of the tank wall to its original shape when cooled by cold molten salt flow in the discharge cycle. Therefore, the steel tank wall is ratcheted at the geometry it reached at the maximum temperature; in other words, the strain ε_L in Eq. (13) is fixed at its maximum value.

When the steel tank subsequently cools in a discharge cycle, the thermal strain is reduced, resulting in an increase in the mechanical strain. The mechanical strain is maximized when the steel reaches its minimum temperature, i.e., ε_T reaches its minimum value in a cycle. For operational safety, this maximum mechanical stress $\sigma_{\max}$ must not exceed the tensile stress of the tank steel σ_y:

$$\sigma_{\max}(x,r) = \alpha_L E\left[T_{2,\max}(x,r) - T_{2,\min}(x,r)\right] < \sigma_y \tag{16}$$

Equation (16) can be rewritten as

$$F_s \cdot \Delta T = \frac{\sigma_y}{\alpha_L \cdot E} \tag{17}$$

where F_s is the factor of safety. Equation (17) provides a design criterion for any potential tank material. For simplicity of calculation, both the expansion coefficient and the modulus of elasticity are assumed to be independent of temperature.

Based on this criterion, the factor of safety F_s associated with thermal ratcheting is maximized by the implementation of highly resilient materials for the steel shell as well as insulation to isolate the shell from the molten-salt temperature fluctuations, provided in the current design by the firebrick. For mechanical analysis of the steel, the coefficient of thermal expansion, modulus of elasticity, and yield strength are assumed to take typical values of 0.00001 K^{-1}, 200 GPa, and 200 MPa, respectively.

2.3 Solution Procedure

Governing equations for the thermal analysis are solved using the commercial computational fluid dynamics (CFD) software, FLUENT 12.1.4 [23]. The thermocline tank and wall domains are discretized into 15750 cells for this finite-volume computation. Spatial discretization of the convective fluxes is performed with a second-order upwind scheme.

Transient discretization is performed with a first-order implicit formulation with a non-dimensional time step of $\Delta\tau = 0.0004$. Time step-independence is verified by comparing results with a reduced non-dimensional time step of $\Delta\tau = 0.0001$. The PISO algorithm is applied for pressure-velocity coupling [24]. A converged solution is considered to have been achieved at each time step when all dimensionless residuals reduce to less than 10^{-4}.

At the start of the simulation, the entire thermocline tank domain is initialized to the hot limit of the molten salt discharge (T_h). In an adiabatic model, this would be a valid initialization as all energy lost through the discharge is recouped in the subsequent charge process. However, since convection and radiation are included at the exposed tank surfaces in the present work, an isothermal condition is not realized at the start of each cycle. Multiple discharge and charge cycles are therefore simulated in succession until a periodic response develops in the entire domain.

Once periodicity is achieved in the domain, the vertical temperature distribution in the steel shell is extracted at multiple times throughout the discharge and charge processes. The maximum and minimum temperatures at each discretized location along the wall are extracted from these instantaneous profiles. These limiting temperatures are then organized into profiles that represent the maximum and minimum values experienced at each location during one complete cycle. The maximum temperature profile determines the final shape and relative position of the tank wall as a result of thermal expansion. Based on this new wall geometry, the minimum temperature profile determines the maximum amount of hoop stress that develops due to the inability of the wall to contract around the reoriented filler region after the settling process.

To solve for the hoop stress, the steel layer is discretized into several deformable solid 2-dimensional elements with the commercial finite element analysis software, ANSYS 12.1 [25].

The non-dimensional size of these elements is $\Delta X = 0.00173$. Temperatures from the maximum profile identified above are applied along the wall to solve for the resultant radial deflections. These deflections are small and assumed to be decoupled from the internal molten-salt behavior. The radial deflections are then fixed while temperatures from the minimum profile are reapplied along the wall to solve for the hoop stress. An alternative approach is to solve for the stress directly from the localized temperature fluctuations with Eq. 16. This second approach is less computationally intensive, but assumes that the remaining principal and shear stresses in the steel shell are negligible relative to the hoop stress.

The fluid flow and heat transfer model was verified against the experimental results from a pilot-scale TES thermocline (2.3MWh) [11] with good agreement [16]. While results from the mechanical analysis could not be validated against experiments due to the absence of reliable data in the literature, the use of two independent approaches – analytical and finite-element – provides a verification.

3. Results and discussion

To investigate tank behavior for various surface conditions and composite wall thicknesses, seven different thermocline tank cases were considered. The composite wall characteristics for each case are summarized in Table 2. In each case, the height and diameter of the filler bed region were both fixed at 12 m to maintain similarity with respect to tank operation. The hot and cold operation limits of the molten salt were also fixed at 450 °C and 293 °C, respectively. The temperature of the surroundings is fixed at 27 °C. In cases 1 through 4, the tank wall configurations were held constant while the convection coefficient was varied between 5 and 10 W/m^2-K and the surface emissivity was varied between 0.5 and 1. In cases 5 through 7, the surface parameters were held constant while the individual thicknesses of the composite wall layers were varied. To account for water cooling at the tank foundation, the bottom wall surface temperature was set at 90 °C in all cases.

As previously discussed, each case required a minimum of five full (discharge and charge) cycles to achieve thermally periodic behavior. Both the discharge and charge processes were computed for six hours of flow time. An additional cycle was required for simulation of case 5 due to the increased thickness of the firebrick layer. Temperature data were extracted from the final discharge and charge processes.

3.1 Flow and temperature fields

Temperature results for case 1 (listed in Table 1) are plotted in Fig. 2 at three separate times during the discharge process. In view of the assumption of axial symmetry, only half of the vertical cross-section view is provided. Early in the discharge ($\tau = 0.513$), only molten salt at the hot temperature limit is present in the upper half of the thermocline. This zone diminishes with time as hot salt is extracted and the thermocline region travels up the filler region. At the

end of the six-hour discharge process ($\tau = 6.516$), the high-temperature salt supply is exhausted and salt is available at progressively cooler temperatures.

It can also be seen from the temperature distributions in the figure that the composite wall region is cooler than the molten salt due to direct exposure to surface convection and radiation. To better illustrate the temperature distribution in the wall, the time-dependent thermal response of the steel shell is plotted in Fig. 3. Temperature profiles at non-dimensional times greater than 6.156 occur during the subsequent charge cycle, and are included to reflect the periodic reheating response of the steel wall. The presence of a phase shift between the wall temperature response and the tank operation is expected due to the inherent thermal mass of the composite wall. Throughout the complete tank operating cycle, the steel wall temperatures remain below the temperature operation limits of the molten salt. Within this smaller temperature range, the temperature variation with time is at a maximum near the center tank height due to the presence of the thermocline region. Near the distributors, this variation is minimal as the traversal of the thermocline region does not extend to the upper and lower extremes of the fillerbed.

While the composite wall is cooled directly due to external losses, molten salt close to the wall is also cooled. As a result, reversed flow of the cooled molten salt can occur along the wall due to buoyancy forces, since the tank discharge velocity in the filler bed is quite low. Occasional swirling and overall disruption of flow uniformity can thus be caused in the filler region despite the inlet flow from the distributor being uniform. As seen in Fig. 2, these effects are most prominent far from the thermocline region where molten-salt temperature gradients are minimal. Early in the discharge, swirling occurs closer to the wall in the large high-temperature region at the top of the fillerbed. This swirling decays with discharge time as the local temperature gradients are eventually dominated by the moving thermocline region. However, a

simultaneous growth of the cold-temperature region occurs at the fillerbed bottom and ultimately results in a new swirl pattern later in the discharge process.

3.2 Outflow Temperature History

In each of the seven cases, the cooling effect from external losses is limited to regions near the tank wall. Thus the discharge performance did not vary to a large extent from case to case. This trend is illustrated in Fig. 4 which shows the average salt temperatures at the discharge port over all cases as a function of time. The discharge temperature variation among the cases is represented by the error bars equal to twice the standard deviation of the sample (*s*), where *s* is defined as:

$$s = \sqrt{\frac{1}{N}\sum_{i=1}^{N}\left(T_i - \bar{T}\right)^2} \tag{18}$$

Though the spread in temperature between the cases increases with discharge time, the salt temperatures remain relatively clustered, with the maximum temperature difference between the seven cases being less than 7% of the total molten-salt operation range at the end of the discharge cycle.

In all cases, high temperature molten-salt outflow is maintained early in the discharge process. Halfway through the discharge cycle, a rapid decline in temperature occurs with an eventual drop to nearly 50% of the molten-salt operation range. The viability of this colder discharge for steam generation depends on the flexibility of the applied Rankine cycle, such as through the use of sliding-pressure operation [26]. In view of the relative insensitivity of the thermocline behavior to details of the tank wall and the heat losses, the recommended approach to prolonging the high-temperature discharge period is to increase the filler region volume.

3.3 Tank Wall Stress

Temperature data from the steel tank shell was extracted from the computed temperature field during the discharge process for stress analysis. As previously discussed, hoop stress may be determined with two separate approaches: (1) by performing an FEA simulation of the steel layer, or (2) by solving for stress directly from the CFD temperature data with Eq. 16. Results from the two approaches applied to the wall temperature data from case 1 are plotted in Fig. 5 for comparison. In the plot, hoop stress is normalized with respect to the yield strength as follows:

$$\omega = \frac{1}{F_s} = \frac{\sigma}{\sigma_y} \tag{19}$$

The two approaches are seen to yield almost identical results. Due to its simplicity, the second approach was adopted for computing the hoop stress for the remaining cases. The normalized results for all seven cases are plotted in Fig. 6.

In cases 1 through 4, the maximum hoop stress is inversely proportional to the heat loss at the tank surface. Among these cases, case 2 experiences the greatest external heat transfer and generates the lowest peak stress value. In contrast, case 3 experiences the least amount of external heat transfer but generates the highest peak stress value. This behavior is due to the sensitivity of the temperature distribution in the composite wall to both external losses and cyclic tank operation. Greater losses at the surface reduce sensitivity to the molten salt fluctuations and dampen cyclic temperature variations along the steel shell. It is also noted that all cases yield normalized peak stress values less than one, with cases 1 through 4 clustered between 0.407 and 0.424. Thus plastic deformation-associated ratcheting would not occur in any of these cases. Since thermal ratcheting is not an issue, case 3 may provide the optimum scenario due to the minimal energy losses to the surroundings.

Even though the tank wall does not reach very high stress levels in cases 1 to 4, further reductions in stress can maximize the factor of safety associated with thermal ratcheting in the event of unexpected increases in heat loss or other unforeseen circumstances. The structure of the composite wall is modified in cases 5 to 7 in terms of the relative thicknesses of the firebrick, steel shell, and ceramic exterior layers, while the surface heat loss conditions are held at the values in case 1. Case 5 experiences the lowest overall peak stress in the steel shell with a normalized value of 0.129 due to the increased firebrick thickness. The added insulation between the filler region and the steel in this case diminishes sensitivity to the fluctuating molten-salt temperatures. Case 6 also exhibits much lower stress levels, with a normalized value of 0.333. The thicker steel layer in this case increases axial conduction which reduces temperature gradients along the shell.

In contrast to the behavior of the firebrick and steel layers, the external ceramic layer thickness must be reduced to decrease hoop stress in the steel shell. A thinner ceramic layer increases the sensitivity of the steel shell to the external losses, which in turn decreases sensitivity to the cyclic molten-salt behavior and dampens temperature fluctuations. This effect is seen in case 7, where the ceramic-layer thickness is reduced by a factor of two compared to the other cases to yield a peak normalized hoop stress of 0.391. However since the peak stress is only reduced by 5% compared to case 1, a larger ceramic layer remains preferable to maximize total insulation between the filler region and the surroundings.

4. Conclusions

A comprehensive thermal model of a molten-salt thermocline tank with a composite wall structure is used to investigate the potential for failure of the tank shell wall by thermal

ratcheting. While hoop stress associated with thermal ratcheting can be resolved with a finite element simulation of the steel shell, nearly identical results can be obtained through simpler analytical strain relations. Various non-adiabatic surface conditions and composite wall geometries are evaluated for their effects on ratcheting potential. The inclusion of external losses at the tank surface affects the flow field in the filler region with reversed flow and swirl patterns being induced in the filler bed during discharge. However, these effects are concentrated near the wall, and do not greatly alter the overall discharge performance.

Hoop stress in the steel shell is a direct consequence of temperature changes generated by the cyclic operation of the thermocline unit. The effects of these cyclic changes on the stresses induced in the steel tank wall are successfully damped by increasing either the surface heat losses or the insulation between the filler region and the steel wall. As surface losses are detrimental to energy storage in the thermocline tank, the recommended solution is to maximize the internal insulation to minimize the potential for thermal ratcheting. Tank wall stresses can also be alleviated by increasing the steel shell thickness to improve axial conduction, but this may lead to impractical tank aspect ratios or excessive radial temperature gradients within the steel.

Nomenclature

C_P specific heat, J kg^{-1} K^{-1}

d diameter of thermocline tank, m

d’ diameter of inlet and outlet ports, m

d_s diameter of filler particles, m

E modulus of elasticity, GPa

$\vec{e}$ unit vector, -

F inertial coefficient, $F = \frac{1.75}{\sqrt{150\varepsilon^3}}$ [27], -

F_s factor of safety, -

g acceleration due to gravity, m/s^2

h height of thermocline tank, m

h’ height of distributor region, m

h_i interstitial heat transfer coefficient, W m^{-2} K^{-1}

K permeability, $K = \frac{d_s^{\,2}\varepsilon^3}{175(1-\varepsilon)^2}$ [28], m^2

k thermal conductivity, W m^{-1} K^{-1}

p pressure, Pa

R non-dimensional tank radius, -

T temperature, K

t time, s

$\vec{u}$ velocity vector, m/s

u_m mean velocity magnitude at inlet to filler region, m/s

X non-dimensional tank height, $X = x/h$, -

Greek

α	thermal diffusivity, m^2/s
α_L	coefficient of thermal expansion, K^{-1}
ε	porosity, -
ε_L	strain, -
ε_r	emissivity, -
μ	viscosity, Pa s
Θ	non-dimensional temperature, $\Theta = \frac{T-T_c}{T_h-T_c}$, -
θ	polar angle, rad
ρ	density, kg/m^3
τ	non-dimensional time, $\tau = t \cdot u_m / h$, -
σ	stress, Pa
σ_r	Stefan-Boltzmann constant, 5.67×10^{-8} W m^{-2} K^{-4}
ω	stress ratio, -

Subscript

1	firebrick
2	steel
3	ceramic
c	cold operation limit
h	hot operation limit
l	liquid salt phase
max	maximum
min	minimum

r	radial direction
ref	reference
s	solid filler phase
w	exterior tank surface
x	x direction
y	yield strength
θ	circumferential direction

References

1. Klaiß H, Köhne R, Nitsch J, Sprengel U, Solar thermal power plants for solar countries – technology, economics, and market potential, Appl Energy 1995;52:165-83.
2. Ravi Kumar K, Reddy KS, Thermal analysis of solar parabolic trough with porous disc receiver, Appl Energy 2009; 86:1804-12.
3. Wu SY, Xiao L, Cao Y, Li YR, A parabolic dish/AMTEC solar thermal power system and its performance evaluation, Appl Energy 2010;87:452-62.
4. Cavallero F, Fuzzy TOPSIS approach for assessing thermal-energy storage in concentrated solar power (CSP) systems, Appl Energy 2010;87:496-503.
5. Yang M, Yang X, Yang X, Ding J, Heat transfer enhancement performance of the molten salt receiver of a solar power tower, Appl Energy 2010;87:2808-11.
6. Kolb G, Hassani V, Performance analysis of thermocline energy storage proposed for the 1 MW Saguaro solar trough plant, Proc of ISEC 2006; Denver, CO.
7. Price H, A parabolic trough solar power plant simulation model, Proc of ISES 2003; Hawaii Island, HI.

8. Kearney and Associates, Engineering evaluation of a molten salt HTF in a parabolic through solar field, NREL Contract No. NAA-1-30441-04; 2001, http://www.nrel.gov/csp/troughnet/pdfs/ulf_herrmann_salt.pdf, as accessed July 2010.

9. Kearney D, Herrmann U, Nava P *et al*., Assessment of a molten salt heat transfer fluid in a parabolic through solar field, J Sol Energy Eng 2003;125:170-6.

10. Brosseau D, Kelton JW, Ray D, Edgar M, Testing of thermocline filler materials and molten-salt heat transfer fluids for thermal energy storage systems in parabolic trough power plants, J Sol Energy Eng 2005;127:109-16.

11. Pacheco JE, Showalter SK, Kolb WJ, Development of a molten-salt thermocline thermal storage system for parabolic trough plants, J Sol Energy Eng 2002;124:153-9.

12. Igari T, Wada H, Ueta M, Mechanism-based evaluation of thermal ratcheting due to traveling temperature distribution, ASME J Pressure Vessel Technol 2000;122:130-8.

13. Russell-Stevens M, Todd RI, Papakyriacou M, Thermal expansion behaviour of ultra-high modulus carbon fibre reinforced magnesium composite during thermal cycling, J Mater Sci 2006;41:6228-36.

14. Faas SE, Thorne LR, Fuchs EA, Gilbersten ND, 10 MWe solar thermal central receiver pilot plant: thermal storage subsystem evaluation – final report, Sandia National Laboratories SAND86-8212; 1986.

15. HITEC heat transfer salt, Coastal Chemical Co., LLC, Brenntag Company, http://www.coastalchem.com/, as accessed July 2010.

16. Yang Z, Garimella SV, Thermal analysis of solar thermal energy storage in a molten-salt thermocline, Sol Energy 2010;84:974-85.

17. Gonzo EE, Estimating correlations for the effective thermal conductivity of granular materials, J Chem Eng 2002;90:299-302.

18. Kolb GJ, Nikolai U, Performance evaluation of molten salt thermal storage systems, Sandia National Laboratories SAND87-3002; 1988.

19. Gabbrielli R, Zamparelli C, Optimal design of a molten salt thermal storage tank for parabolic trough solar power plants, J Sol Energy Eng 2009;131:041001-10.

20. Launder BE, Spalding DB, Lectures in mathematical models of turbulence. London, England: Academic Press; 1972.

21. Wakao N, Kaguei S, Heat and mass transfer in packed beds. New York: Gordon and Beach; 1982.

22. Yang Z, Garimella SV, Molten-salt thermal energy storage in thermocline under different environmental boundary conditions, Appl Energy, doi:10.1016/j.apenergy.2010.04.024.

23. FLUENT 12.1.4 Documentation, Fluent Inc., as accessed July 2010.

24. Issa RI, Solution of implicitly discretized fluid flow equations by operator splitting, J Comput Phys 1986;62:40-65.

25. ANSYS 12.1 Documentation, ANSYS Inc., as accessed July 2010.

26. Solar Thermocline Storage Systems: Preliminary Design Study. EPRI, Palo Alto, CA: 2010. 1019581.

27. Krishnan S, Murthy JY, Garimella SV, A two-temperature model for analysis of passive thermal control systems, J Heat Transfer 2004;126:628-37.

28. Beckermann C, Viskanta R, Natural convection solid/liquid phase change in porous media, Int J Heat Mass Transfer 1988;31:35-46.

Table 1. Thermal transport properties of composite wall layers.

Material	**k (W/m-K)**	**ρ (kg/m^3)**	**C_P (J/kg-K)**
Firebrick	1	2000	1000
Steel	60	8000	430
Ceramic	1	1000	1000

Table 2. Summary of the cases considered with different wall structural parameters and heat loss conditions.

Case	**h (W/m^2-K)**	**ε_r**	**δ_{fb} (m)**	**δ_{cs} (m)**	**δ_{cer} (m)**
1	5	1	0.1	0.02	0.05
2	10	1	0.1	0.02	0.05
3	5	0.5	0.1	0.02	0.05
4	10	0.5	0.1	0.02	0.05
5	5	1	0.2	0.02	0.05
6	5	1	0.1	0.04	0.05
7	5	1	0.1	0.02	0.025

Figure Captions

Figure 1. Schematic illustration of the thermocline tank with a composite wall consisting of firebrick (1), steel (2), and ceramic (3).

Figure 2. Normalized temperature and flow fields of the case 1 thermocline tank at early ($\tau = 0.513$), midpoint ($\tau = 3.078$), and end ($\tau = 6.156$) stages of the discharge cycle.

Figure 3. Temperature profiles along the steel shell (case 1).

Figure 4. Molten-salt outflow temperature during thermocline tank discharge (averaged over all cases). Variation between the cases is represented with error bars equal to two standard deviations (Eq. 18).

Figure 5. Comparison of hoop stresses determined for case 1 using finite element analysis (FEA) and analytical strain relations.

Figure 6. Hoop stress profiles along the fillerbed height for all cases (see Table 2).

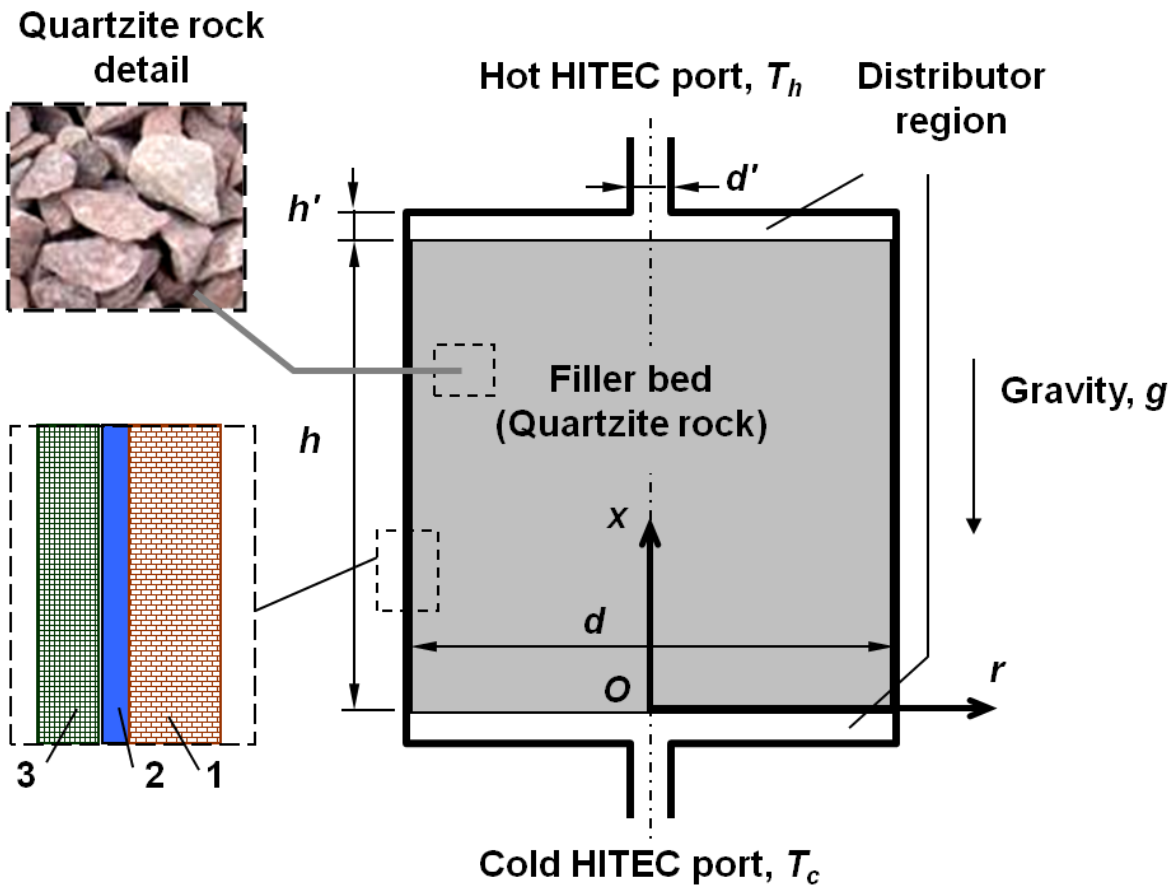

Figure 1 Schematic illustration of the thermocline tank with a composite wall consisting of firebrick (1), steel (2), and ceramic (3).

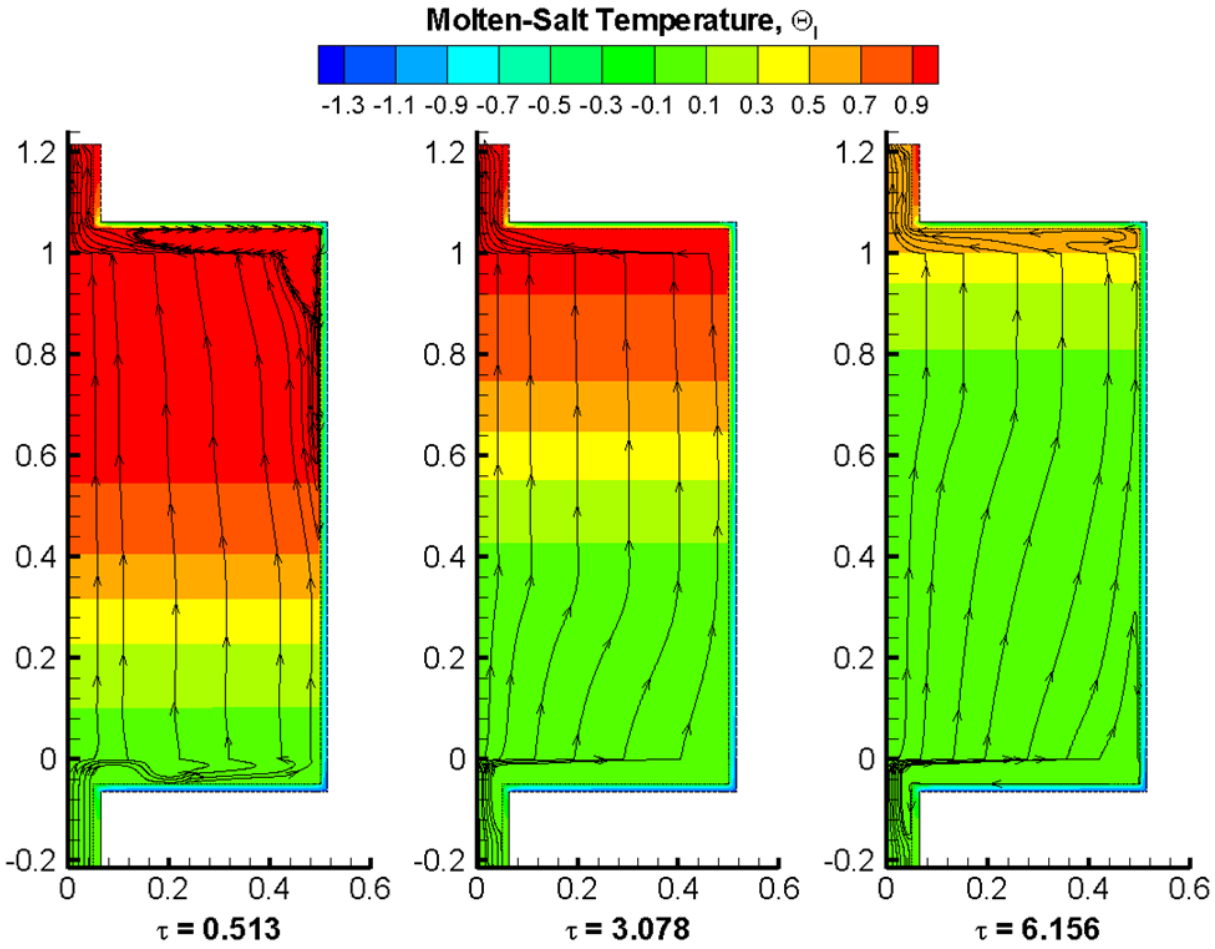

Figure 2 Normalized temperature and flow fields of the case 1 thermocline tank at early (τ = 0.513), midpoint (τ = 3.078), and end (τ = 6.156) stages of the discharge cycle.

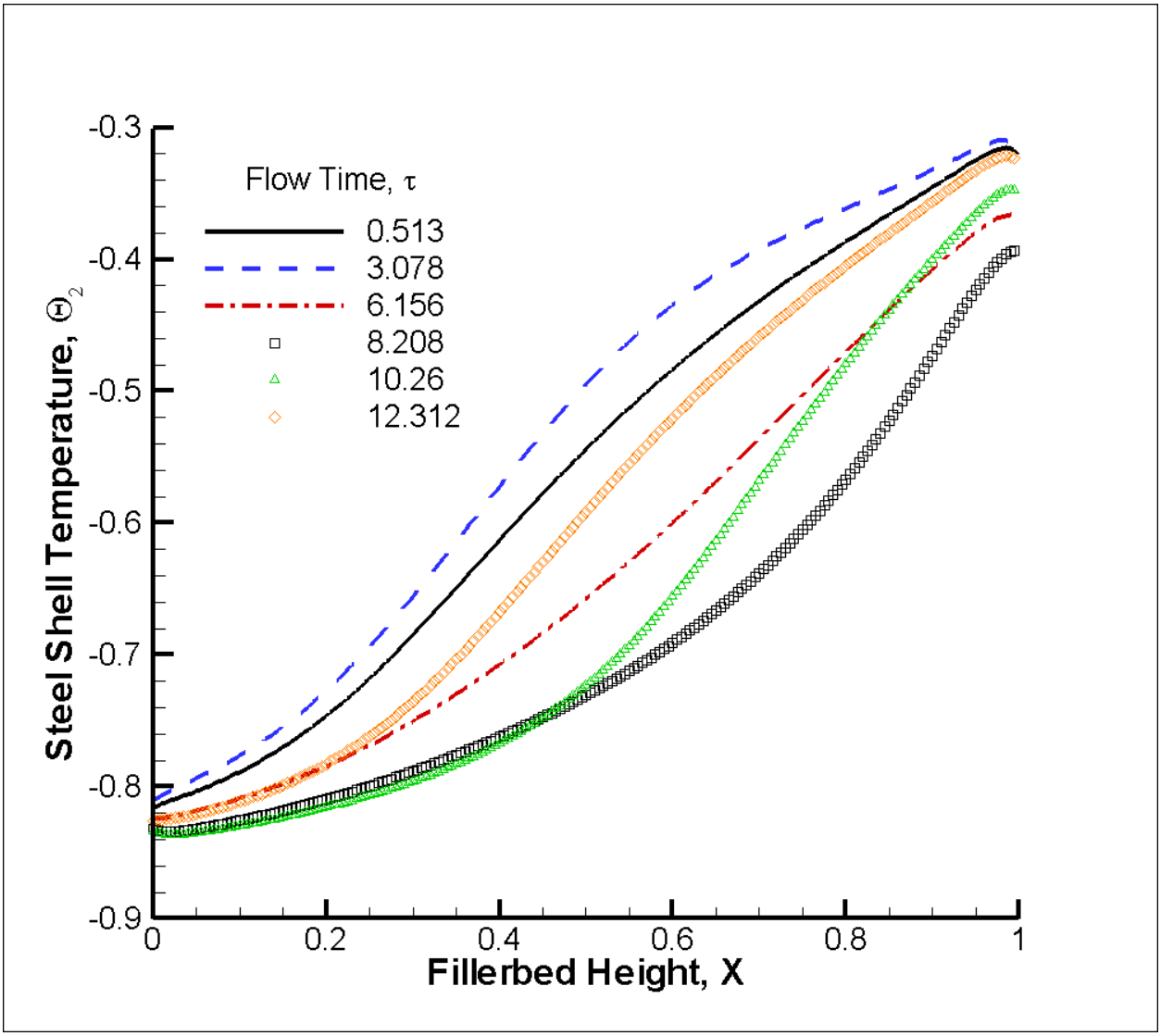

Figure 3 Temperature profiles along the steel shell (case 1).

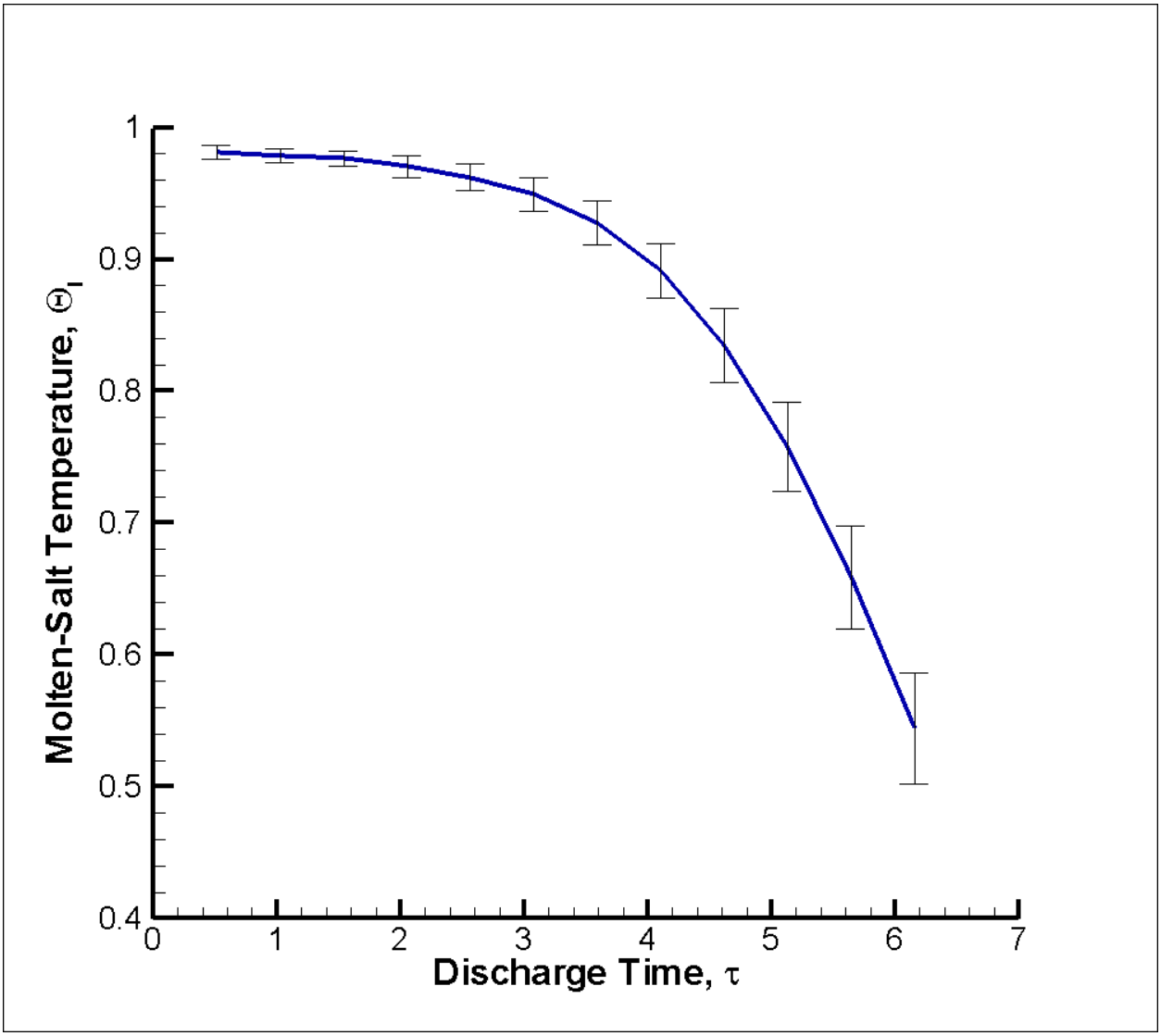

Figure 4 Molten-salt outflow temperature during thermocline tank discharge (averaged over all cases). Variation between the cases is represented with error bars equal to two standard deviations (Eq. 18).

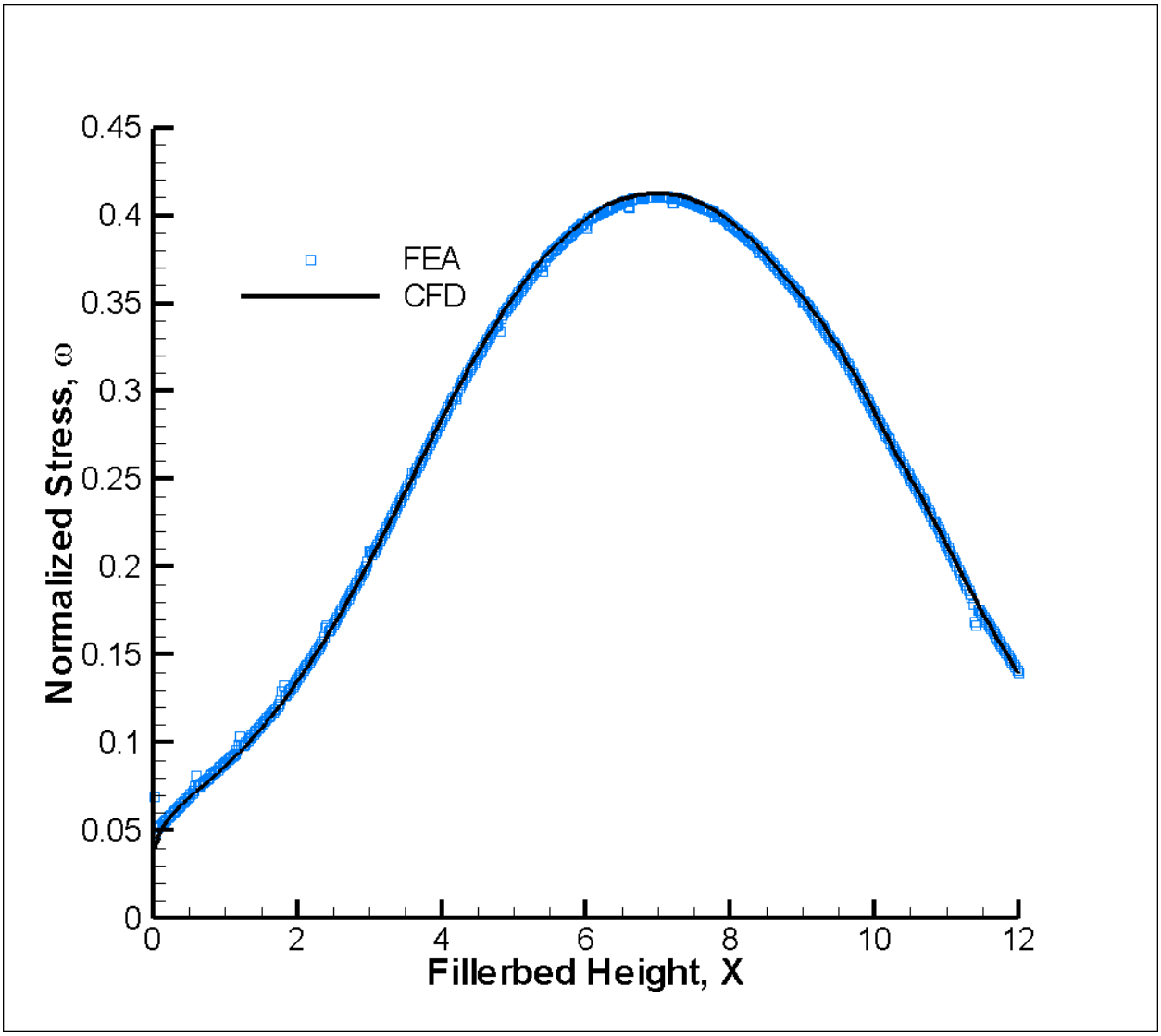

Figure 5 Data comparison of hoop stress determination (case 1) using finite element analysis (FEA) and analytic stress relations (CFD).

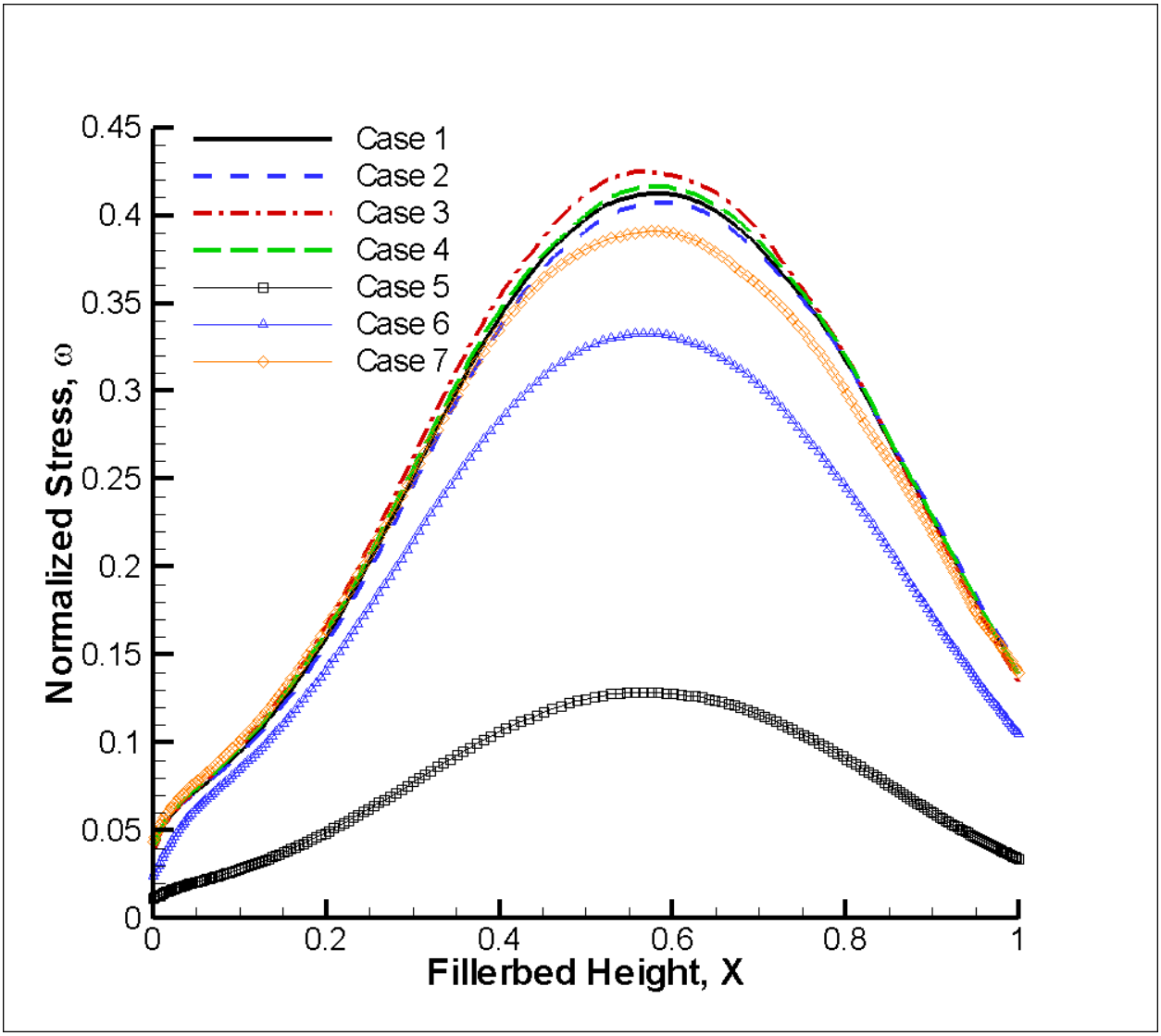

Figure 6 Hoop stress profiles along the fillerbed height for all cases (see Table 2).